IEEE Access
Multidisciplinary | Rapid Review | Open Access Journal

Received March 2, 2019, accepted April 7, 2019, date of publication April 24, 2019, date of current version May 2, 2019.

Digital Object Identifier 10.1109/ACCESS.2019.2911696

Fast Compressive Sensing-Based SAR Imaging Integrated With Motion Compensation

WEI PU, (Student Member, IEEE), YULIN HUANG, (Member, IEEE), JUNJIE WU, (Member, IEEE), HAIGUANG YANG, (Member, IEEE), AND JIANYU YANG, (Member, IEEE)

School of Information and Communication Engineering, University of Electronic Science and Technology of China, Chengdu 611731, China

Corresponding author: Junjie Wu (junjie_wu@uestc.edu.cn)

This work was supported in part by the National Natural Science Foundation of China under Grant 61401078 and Grant 61771113.

ABSTRACT Recently, compressive sensing (CS) has been applied in synthetic aperture radar (SAR) imaging, which is increasingly in the focus of study and shows great potential. In CS-based SAR imaging, motion errors of the moving platform introduce inaccuracies in the observation model, which cause various degradations in the final images. To accomplish accurate motion compensation during CS-based SAR imaging, we propose a fast CS-based SAR imaging integrated with motion compensation method. First, CS-based imaging based on the utilization of inverse observation deduced from the inversion of conventional imaging procedures is applied, which is much more computational efficient than the exact observation model. Then, an improved inverse observation model integrated with motion compensation is derived. In the improved model, spatially variant azimuth phase errors are taken into consideration. Joint SAR imaging and motion compensation are formulated as a sparse recovery problem and solved in an iterative way, wherein each iteration both image formation and motion compensation are carried out. The processing of SAR data shows that the proposed method can obtain better focused images compared with the existing SAR imaging and motion compensation methods.

INDEX TERMS Radar imaging, synthetic aperture radar.

I. INTRODUCTION

Synthetic aperture radar (SAR) [1], [2] enhances and improves the capability of information acquisition, which produces high spatial resolution images from a moving platform. Some theories for SAR image reconstruction have been developed, such as range-Doppler (RD), chirp-scaling and back-projection (BP) and so on. The conventional imaging algorithms are efficient, but the Nyquist sampling theory requires that the SAR signal should be sampled at a frequency at least twice its bandwidth to be able to reconstruct it exactly for both range and azimuth directions. With the resolution becoming increasingly finer and imaging swath increasingly larger, SAR system needs more and more measurements and storage. Unfortunately, however, the current system hardware always hampers such large-amount and high-dimensional application.

A newly introduced theory of compressed sensing (CS) presents that, we can reconstruct a sparse or compressible signal accurately from a highly incomplete measurements utilizing CS theory [4]–[6]. A lot of literatures [7]–[10] were proposed to apply the CS theory in conventional SAR system which can solve the problem of high amount of sampled data. If modeling the data acquisition procedure into an exact observation, the number of measurements can be much smaller than the equivalent number of Nyquist rate samples [11].

In practical applications, due to the effect of platform vibration, wind field, and turbulence, the platform might greatly deviate from the ideal straight trajectory [12]–[17], and therefore, the exact observation models often have uncertainties. These uncertainties degrade the image quality drastically during imaging. In principle, it is possible to correct the uncertainties stemming form motion errors utilizing the motion measurement data provided by an ancillary instrument such as inertial navigation system (INS) and global positioning system (GPS). However, measurement uncertainties on the data would limit the accuracy. Thus, motion compensation based on the raw data, which is

The associate editor coordinating the review of this manuscript and approving it for publication was Guolong Cui.

also called autofocus, should be used to improve the image quality.

Various studies have been presented on the autofocus problem [19], [21]–[26]. However, conventional autofocus methods can not be utilized in the CS-based imaging algorithms directly. Several CS-based imaging formation methods considered the motion errors. In [27], a sparsity-driven autofocus method is proposed to deal with the SAR image formation from the data corrupted by motion error, but spatial-variance of the motion errors is neglected. To solve this problem, phase errors are divided into three subcategories, i.e., 1-D phase, 2-D separable, and 2-D nonseparable errors, and they are corrected by using a nonquadratic regularization approach [28]. The compensation of 2-D separable and 2-D nonseparable errors can eliminate the range-variance of motion errors. In [29], the authors focus on the case when the range-variant phase error arises from the incorrect measurement of the platform motion parameters.

However, another serious drawback of the CS-based imaging algorithm is that compared with the traditional imaging methods, the CS-based imaging algorithms need larger computational complexity. In order to deal with such a problem, instead of exact observation model, some CS-based imaging algorithms are proposed based on approximation observation [30], [31]. As the focused SAR image can be viewed as the output of the imaging operator performed on the SAR echo, we can use an inverse observation model derived from the inversion of traditional imaging algorithms to replace the exact observation. Based on such inverse observation, the SAR image can be reconstructed in a more efficient way. The autofocus methods in CS-based SAR imaging mentioned above cannot be directly utilized integrated with the inverse observation model imaging algorithms.

In this paper, we propose a novel fast CS-based SAR imaging integrated with motion compensation. Firstly, motion errors property of the SAR is analyzed, and it can be concluded that only range-variance of the motion errors should be taken into consideration, and the azimuth-variance can be neglected. Based on this conclusion, a range-variant autofocus is added into the inverse observation model. After that, the proposed approach is implemented through SAR image reconstruction and range-variant phase error estimation by solving a sparse recovery problem. Note that the motion compensation and image reconstruction are carried out simultaneously in the proposed approach. As motion errors has been eliminated in the inverse observation, the image quality will be greatly improved in contrast to the existing methods. The main contribution of the proposed approach is

1) We propose an improved inverse observation model combined with a spatially-variant motion compensation, which has the advantage of greatly increasing the imaging quality in practical application.
2) Correspondingly, a block coordinate descent scheme is proposed to solve the estimation problem in the improved inverse observation model, where motion errors and the RCS information of the image scene are estimated simultaneously in the proposed approach.

The rest of this paper is organized as follows. The fast CS-based SAR imaging algorithm using inverse observation and autofocus method is introduced. Section III gives the motion error model of SAR, and analyzes the motion errors' spatial-variance property. In section IV, a fast CS-based SAR imaging integrated with motion compensation method is derived in detail. Numerical results are given in Section V. Section VI concludes this paper.

II. RELATED WORK

This section briefly introduces two preceding works, CS-based SAR imaging using exact observation and fast CS-based SAR imaging using inverse observation.

A. CS-BASED SAR IMAGING USING EXACT OBSERVATION

In SAR systems, suppose the radar transmits linear frequency modulated (FM) pulses at a constant rate. Let x and y denote the range and azimuth position of the reconstructed SAR image, which be indexed by $m = 1, 2, \cdots, N_r$ and $n = 1, 2, \cdots, N_a$, respectively, where M and N are the sample number with respect to range and azimuth direction. Suppose τ and t represent the range and azimuth time, respectively, and $i = 1, 2, \cdots, I$ and $q = 1, 2, \cdots, Q$ index the the range and azimuth time, where I and Q are the sample number of range and azimuth time, respectively. Let $s_0(\tau_i, t_q, x_m, y_n)$ represent the received signal of the qth pulse in the ith sequence from the target located at (x_m, y_n), and it can be written as shown in (1).

$$\begin{aligned} s_0(\tau_i, t_q, x_m, y_n) = {} & \delta(x_m, y_n)\omega_r\left(\tau_i\right)\omega_a\left(t_q\right) \\ & \cdot \exp\left\{-j\pi k_r\left(\tau_i - \frac{r(t_q, x_m, y_n)}{c}\right)^2\right\} \\ & \cdot \exp\left\{-j4\pi f_c \frac{r(t_q, x_m, y_n)}{c}\right\}. \end{aligned} \tag{1}$$

In (1), ω_r and ω_a are range and azimuth envelope, $\delta(x_m, y_n)$ denotes the reflector coefficient for the target located at (x_m, y_n), $r(t_q, x_m, y_n)$ is the instantaneous slant range from image position (x_m, y_n) to the moving platform, f_c is the carrier frequency, c is the speed of light, and k_r is range chirp FM rate.

Assume the received signal at the qth pulse of the ith sequence for whole area illuminated by the beam is represented by $s(\tau_i, t_q)$. $s(\tau_i, t_q)$ can be written as

$$s(\tau_i, t_q) = \sum_m \sum_n s_0(\tau_i, t_q, x_m, y_n). \tag{2}$$

By setting

$$\begin{aligned} \varphi(\tau_i, t_q, x_m, y_n) = {} & \omega_r\left(\tau_i\right)\omega_a\left(t_q\right) \\ & \cdot \exp\left\{-j\pi k_r\left(\tau_i - \frac{r(t_q, x_m, y_n)}{c}\right)^2\right\} \\ & \cdot \exp\left\{-j4\pi f_c \frac{r(t_q, x_m, y_n)}{c}\right\}, \end{aligned} \tag{3}$$

the SAR echo data $s(\tau_i, t_q)$ can be rewritten as

$$s(\tau_i, t_q) = \sum_m \sum_n \varphi(\tau_i, t_q, x_m, y_n)\delta(x_m, y_n). \tag{4}$$

According to (4), the relationship between the received echo and reflector coefficients can be rewritten as

$$y' = H'x, \tag{5}$$

where $y' = vec\,(s(:,:))$ is the vector representation of the echo, $x = vec(\delta(:,:))$ denotes the vector representation of the the reflector coefficient, and H is the system matrix (6), as shown at the bottom of this page. In (6), $a_{i,q}$ is

$$a_{i,q} = \left[vec\left(\varphi(\tau_i, t_q, :, :)\right)\right]^H, \tag{7}$$

for any $i = 1, 2, \cdots, I$ and $q = 1, 2, \cdots, Q$.

In (5), the received SAR echo y and system matrix H are known, and we need to recover the reflector coefficient vector x by solving the linear equations. In conventional SAR system, the sampling frequencies of both azimuth and range direction should be twice than the corresponding bandwidths according to the requirement Nyquist theory, and we usually have $IQ \geq MN$.

However, this requirement needs too many sampling amount especially in the high resolution and large swath case. Fortunately, the framework of the CS theory shows that x is recoverable if x is sparse or compressible. To utilize the CS-based approaches, random sampling should be employed on the received data, which is equivalent to performing a random selection on the uniform sampled data. The random selection operation can be represented by a 0-1 matrix Ξ of size $P \times IQ$, where $P \ll IQ$. By setting $H = \Xi H'$ as the measurement matrix, we can get the relationship between the random sampled video SAR echo y and the reflector coefficient vector to be reconstructed x as

$$y = Hx. \tag{8}$$

(8) model the SAR echo acquisition into an exact observation. If x is sparse, we can recover x from the exact observation by solving a following minimum l_0 optimization problem as

$$\arg\min_x |x|_0, \qquad s.t. \quad y = Hx, \tag{9}$$

where $|\cdot|_0$ denotes l_0 norm, which returns the number of nonzero elements in the vector. The optimization problem in (9) is non-deterministic polynomial (NP) hard. One solution is to use the greedy strategies like Orthogonal Match Pursuit (OMP) or some. Another approaches taken in CS are usually to solve a relaxed version

$$\arg\min_x |x|_1, \qquad s.t. \quad y = Hx, \tag{10}$$

where $|\cdot|_1$ denotes a l_1 norm, which returns the sum of the absolute values of all the elements in the vector. The solution to (9) is often known as Basis Pursuit (BP) [32], which can be solved by linear programming methods. It has been shown that under certain conditions on system matrix H and the sparsity of x, the solution to both and will coincide [33].

In addition to the sparsity of x, another sufficient condition to recover x, is known as the Restricted Isometry Property (RIP) [4], [34], [35]. The RIP of SAR system has been verified in some previous literatures [7], [9].

Note that in the practical application, the reflector coefficient vector x is not naturally sparse. But in most cases, we can find a transform to make most of the coefficients in the transform domain to be zero or very small. In this situation, we need to use a sparse transform in the CS scheme [36].

B. FAST CS-BASED SAR IMAGING USING INVERSE OBSERVATION

In the imaging algorithms of SAR processing, it is known that the computational complexity order of the frequency-domain imaging methods is lower than it of the CS-based imaging algorithm using exact observation. Inspired by this, literatures in [30] and [31] tried to combine the CS-based SAR imaing with traditional frequency-domain imaging algorithms, and accelerate the CS-based SAR imaging procedures to achieve a comparable (at the same order) complexity with the frequency-domain imaging methods.

Taking RD algorithm as an example, the flowchart of the RD algorithm is shown in Fig. 1.

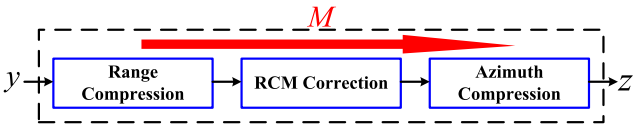

FIGURE 1. Flowchart of the RD imaging algorithm.

The procedure of RD algorithm consists of three main steps: 1) range compression, 2)residual range cell migration correction, and 3) azimuth compression. Assuming that M denotes the matrix representation of the RD algorithm and z is the vector representation of the final focused SAR image, the relationship between the SAR echo y and the final focused SAR image z is

$$z = My. \tag{11}$$

In a compact form, the imaging procedure M, operated on 2-D array, can then be expressed as follows

$$M = F_t^H P_t F_\tau^H R F_t P_\tau F_\tau. \tag{12}$$

where F_t and F_τ denote the Discrete Fourier transform with respect to azimuth and range directions, respectively,

$$H' = \left[\, a_{1,1}\ a_{1,2}\ \cdots\ a_{1,Q}\ a_{2,1}\ a_{2,2}\ \cdots\ a_{2,Q}\ \cdots\ a_{I,1}\ a_{I,2}\ \cdots\ a_{I,Q,t}\ \right]^H \tag{6}$$

F_t^H and F_τ^H represent the inverse Discrete Fourier transform with respect to azimuth and range directions, P_t and P_τ are the phase multiplication matrixes of frequency-domain matched filter operations along azimuth and range, and R denotes the phase multiplication matrix of the range cell migration correction, where the specific definitions can be found in [30].

With such concrete procedures in RD algorithm, the inverse of the RD algorithm can be acquired by taking the inverse of each procedure. The Discrete Fourier transformations and the inverse Discrete Fourier transformations can be easily obtained as they are mutually conjugate transpose to each other. The inversion of phase multiplication of matrixes P_t, P_τ, and R is the multiplication of their conjugate phase matrixes. Then, the inversion of the RD algorithm can be formulated as the inversion observation model as follows

$$y = M^{-1}z, \tag{13}$$

where

$$M^{-1} = F_\tau^H P_\tau^H F_t^H R^H F_\tau P_t^H F_t. \tag{14}$$

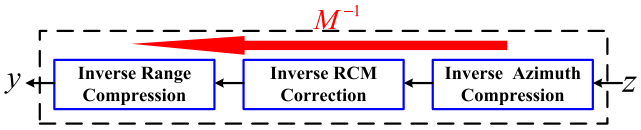

FIGURE 2. Flowchart of the inversion of RD imaging algorithm.

The flowchart of the inversion of RD imaging algorithm is shown in Fig. 2. By employing a random selection processing, (13) is changed into

$$y = \Xi M^{-1}z. \tag{15}$$

Mathematically, the reason why the computational efficiency of the CS based method using the inversion observation model is higher than it using the exact observation model lies in the fact that M^{-1} is a block diagonal matrix, which contains a large number of 0 elements. Therefore, using M^{-1} to employ the CS based SAR imaging is of less computational cost than using matrix H, which is a matrix with all elements not equaling to 0. The relations between exact observation and inverse observation is shown in Fig. 3.

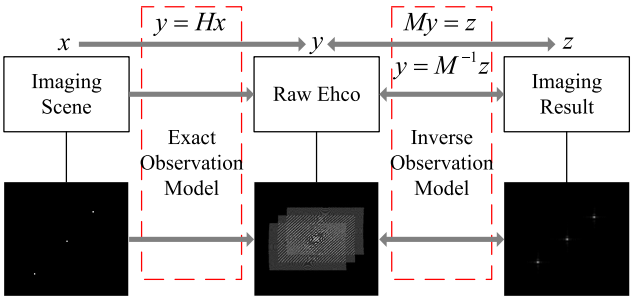

FIGURE 3. Relations between exact observation and inverse observation.

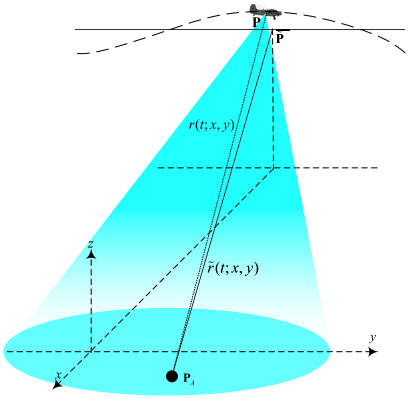

FIGURE 4. Imaging geometry configuration of SAR.

As the imaging results z is an approximation to the reflector coefficient vector x, the sparsity or compressibility of z and x are almost the same. As the RIP property of the inverse imaging matrix M^{-1} has been verified in [31], it's possible to use the inverse observation model to derive a CS-based imaging algorithm. The corresponding optimization problem is formulated as

$$\arg\min_z |z|_0, \qquad s.t. \quad y = \Xi M^{-1}z. \tag{16}$$

The reconstruction problem expressed in (16) can be solved by a convex program to the relaxed version of l_0 norm or greedy algorithms as well.

III. SPATIAL-VARIANCE PROPERTY OF MOTION ERRORS

In this section, the geometry configuration of the SAR system in the presence of motion errors is presented in the first subsection. Then, based on the geometry configuration, spatial-variance property of motion errors is analyzed in the second subsection.

A. GEOMETRY

In the nominal condition without any motion errors, the geometry configuration of SAR is shown in Fig. 1. Transmitter and receiver are assumed to move along y axis with the same velocity V. The direction of x axis denotes range, and the direction of y represents azimuth in this paper. The azimuth time t is chosen to be zero at the composite beam center crossing time of the reference target. The position vector of the reference target is $\mathbf{p}_0 = [0 \quad 0 \quad 0]^T$, and target A is an arbitrary point target in the imaging area $\mathbf{p}_A = [x \quad y \quad z]^T$. In the condition without motion errors, the position vector of the platform at the azimuth time t_q is

$$\widetilde{p} = [x_T \quad Vt_q + y_T \quad z_T]^T \tag{17}$$

Accounting for the trajectory deviations stemming from motion errors and elevation variation, $\mathbf{p}_T$ and $\mathbf{p}_R$ denote the actual instantaneous position vector of the transmitter and receiver, respectively. The explicit expressions are

$$p = \widetilde{p} + e, \tag{18}$$

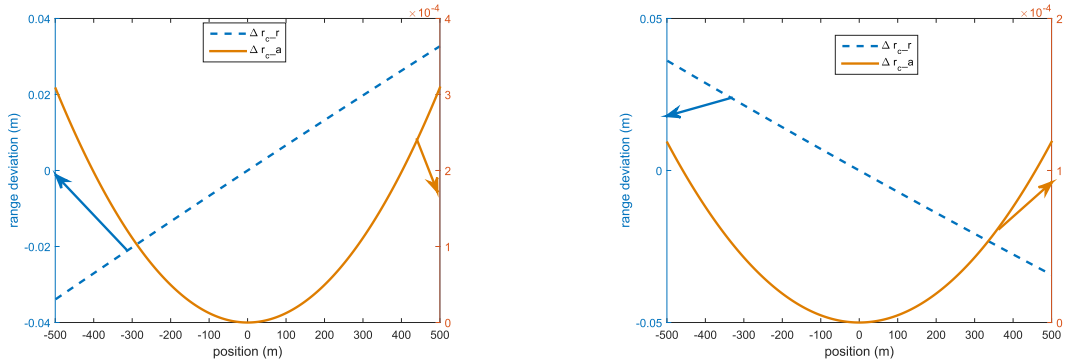

FIGURE 5. Spatial-variance of $\Delta r_{T_c}(t_q; x, y)$ in the presence of different cross-track errors. (a)$\Delta x_T(t_q) = 1.2m$, $\Delta z_T(t_q) = -0.8m$. (b)$\Delta x_T(t_q) = -0.6m$, $\Delta z_T(t_q) = 1m$.

where $\mathbf{e}$ represent the motion errors vector of the platform.

$$\mathbf{e} = [\Delta x_T(t_q) \quad \Delta y_T(t_q) \quad \Delta z_T(t_q)]^T \tag{19}$$

The actual range history of the target A can be expressed as

$$r(t_q; x_m, y_n) = \|\mathbf{p} - \mathbf{p}_A\| \tag{20}$$

The nominal range history for target A is

$$\widetilde{r}(t_q; x_m, y_n) = r|_{\mathbf{e}=[0 \quad 0 \quad 0]^T} \tag{21}$$

Then, the range history deviations stemming from the motion errors can be calculated as

$$\Delta r(t_q; x_m, y_n) = r(t_q; x_m, y_n) - \widetilde{r}(t_q; x_m, y_n). \tag{22}$$

B. SPATIAL-VARIANCE PROPERTY OF MOTION ERRORS

The motion errors are three-dimensional, i.e. x, y, z. The errors in the y-direction account for along-track nominal velocity changes that are generally compensated via an on-board adjustment of the pulse repetition frequency or, via azimuth re-sampling of raw data. Therefore, the effect of the along-track velocity errors is assumed to be negligible, and we focus on the property of the motion errors in the cross-track direction [17].

Range deviations stemming from the cross-track errors is shown as

$$\Delta r_c(t_q; x_m, y_n) = r_c(t_q; x_m, y_n) - \widetilde{r}(t_q; x_m, y_n), \tag{23}$$

where r_c denotes the range history in the presence of cross-track motion errors. In (24), as shown at the bottom of this page, the range- and azimuth-dependent component of Δr_c are expressed by Δr_c_r and Δr_c_a, respectively.

To analyze the spatial-variance properties of Δr_c, simulations with two different cases are conducted (considering an X band system, $\lambda = 0.03m$).The initial position vector the platform is $[-8, 0, 10]km$.

Fig. 5 give the spatial-variance of range deviation Δr_c at t_q with two different cases. The range deviation of the transmitter Δr_c varies with range position linearly, and with azimuth position quadratically. However, the azimuth-variant component is much smaller than the range-variant component. Δr_c_a is within $10^{-3}m$ for both two cases, and it can be neglected during imaging processing [37].

From the analyses of the spatial-variance property of motion errors, it can be concluded that both the azimuth- and range-variance of range deviation should be taken into consideration in SAR imaging.

IV. FAST CS-BASED SAR IMAGING INTEGRATED WITH MOTION COMPENSATION

Based on the conclusion of the spatial-variance property of the motion errors, a range-variant phase error correction procedure is added into the inverse observation model. Utilizing the improved inverse observation, a block coordinate descent optimization scheme is carried out to realize the estimation of the range-variant phase errors and final image reconstruction at the same time.

A. IMPROVED INVERSION MODEL

To cope with the range-variant motion errors, we should multiply different phase errors in different range gates for the 2-dimensional time domain data before azimuth compression and after RCM correction. The flowchart of the RD imaging algorithm with motion compensation is shown in Fig. 6. Suppose the 2-dimensional time domain data before azimuth compression and after RCM correction is denoted as $s_0(\tau_i, t_q)$, and the data after motion compensation is $s_1(\tau_i, t_q)$.

$$\begin{cases} \Delta r_c\_r(t_q; x_m, y_n) = \Delta r_c(t_q; x_m, y_n)|_{y_n=0} - \Delta r_c(t_q; x_m, y_n)|_{x_m=0, y_n=0}, \\ \Delta r_c\_a(t_q; x_m, y_n) = \Delta r_c(t_q; x_m, y_n)|_{x_m=0} - \Delta r_c(t_q; x_m, y_n)|_{x_m=0, y_n=0}. \end{cases} \tag{24}$$

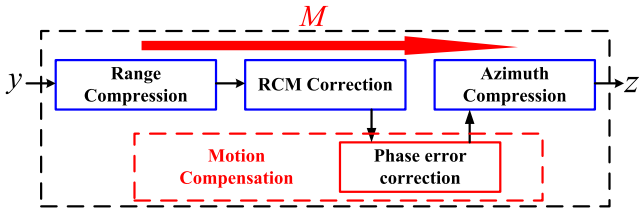

FIGURE 6. Flowchart of the RD algorithm with motion compensation.

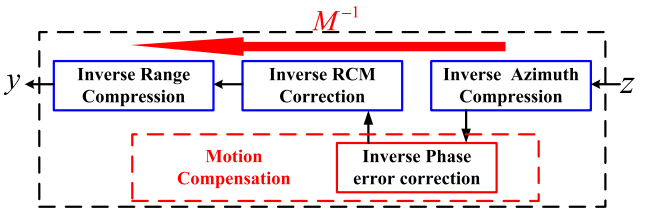

FIGURE 7. Flowchart of the inversion of RD algorithm with motion compensation.

Then,

$$s_1(\tau_i, t_q) = s_0(\tau_i, t_q)e^{j\phi(\tau_i, t_q)}. \tag{25}$$

In a matrix manner, (25) can rewritten as

$$v_1 = v_0 e^{j\Phi}, \tag{26}$$

where v_0 and v_1 are the vector representation of $s_0(\tau_i, t_q)$ and $s_1(\tau_i, t_q)$, respectively, and Φ is the matrix representation of the correction phase. The concrete definitions of v_0 and v_1 are $v_0 = \mathrm{vec}(s_0(:,:))$, $v_1 = \mathrm{vec}(s_1(:,:))$, respectively, and expression of Φ in (27), as shown at the bottom of this page. Noted that in (27), we need to employ a range-variant motion compensation, which multiplies a correction phase for each sampling of the SAR data, according to the conclusion in subsection III.B. In some certain cases, if the imaging scene is small in width of range direction, or we don't need a SAR image with very high quality, we can just use the spatial-invariant phase correction matrix Φ' in (28), as shown at the bottom of this page. Compared with (27), we reduce the dimension of phase error correction from IQ to Q, and increase the computational efficiency in (28). In this paper, we still treat the phase errors as range-variant, which is more common in practical application.

Then, the imaging matrix M is changed into

$$M = F_t^H P_t F_t e^{j\Phi} F_t^H F_\tau^H R F_t P_\tau F_\tau. \tag{29}$$

Accordingly, matrix representation of the inversion of RD algorithm with range-variant phase error correction is

$$M^{-1} = F_\tau^H P_\tau^H F_t^H R^H F_\tau F_t e^{-j\Phi} F_t^H P_t^H F_t. \tag{30}$$

The flowchart of the inversion of RD algorithm with motion compensation is shown in Fig. 7.

It should be noted that in (30), phase error matrix Φ can be calculated by motion measurement data. But in most practical applications, the accuracy of the motion measurement is not high enough to meet the requirement of motion compensation in high-resolution SAR imaging. Therefore, phase error matrix Φ needs to be estimated as well as the final focused imaging result y in the CS-based imaging process. The imaging problem in (16) is changed into

$$\arg\min_{z,\Phi} |z|_0, \qquad s.t. \quad y = M_1 e^{-j\Phi} M_2 z, \tag{31}$$

where $M_1 = \Xi F_\tau^H P_\tau^H F_t^H R^H F_\tau F_t$ and $M_2 = F_t^H P_t^H F_t$. In M_1, random sampling have been employed on the received data as we have multiplied the random selection matrix Ξ.

B. BLOCK COORDINATE DESCENT OPTIMIZATION SCHEME

To solve (31), we use the relax version l_1 norm to replace l_0 norm and pose the optimization problem as the minimization of the following cost function:

$$J(z, \Phi) = \left\| y - M_1 e^{-j\Phi} M_2 z \right\|_2^2 + \lambda \|z\|_1, \tag{32}$$

where λ is the regularization parameter, which trades off the reconstruction precision and the sparsity of the solutions obtained. The regularization parameter has a substantial impact on the imaging result. Fortunately, as a part of the regularization theory, the optimally has been resolved in [38], whenever the problemâĂŸs sparsity is known.

Then, a block coordinate descent optimization scheme is applied to minimize the cost function F. In an iterative manner, the imaging result z and phase error Φ are estimated consecutively in each iteration. The algorithm is summarized as follows.

Algorithm 1

Input: Initialize $p = 0$

Repeat

Step 1: $\hat{z}^{p+1} = \arg\min_z J\left[\hat{\Phi}^p, z\right]$.

Step 2: $\hat{\Phi}^{p+1} = \arg\min_\Phi J\left[\Phi, \hat{z}^{p+1}\right]$.

$p \leftarrow p + 1$ until $e = \left\| \frac{\hat{z}^{p+1} - \hat{z}^p}{\hat{z}^p} \right\|$ is less than a predetermined threshold δ.

In this paper, the value of the threshold δ is chosen as 10^{-4}.

$$\Phi = \mathrm{diag}\left[\phi(\tau_1, t_1) \cdots \phi(\tau_I, t_1)\ \phi(\tau_1, t_2) \cdots \phi(\tau_I, t_2) \cdots \phi(\tau_1, t_Q) \cdots \phi(\tau_I, t_Q)\right] \tag{27}$$

$$\Phi' = \mathrm{diag}\left[\underbrace{\phi(t_1) \cdots \phi(t_1)}_{I}\ \underbrace{\phi(t_2) \cdots \phi(t_2)}_{I} \cdots \underbrace{\phi(t_Q) \cdots \phi(t_Q)}_{I}\right] \tag{28}$$

$$W(z) = diag\left[1+\lambda(|z_1|^2+\beta)^{-\frac{1}{2}}, 1+\lambda(|z_2|^2+\beta)^{-\frac{1}{2}}, \cdots, 1+\lambda(|z_D|^2+\beta)^{-\frac{1}{2}}\right]. \quad (36)$$

In the block coordinate descent optimization, p denotes the iteration number. $\hat{z}^p$ and $\hat{\Phi}^p$ represent the estimation of z and Φ in the pth iteration. In the first step of the $p+1$th iteration, the optimization is

$$\hat{z}^{(p+1)} = \arg\min_z \left\| y - M_1 e^{-j\hat{\Phi}^p} M_2 z \right\|_2^2 + \lambda \|z\|_1. \quad (33)$$

In (33), a smooth approximation is used to avoid the non-differentiability of the l_1-norm

$$\|z\|_1 \approx \sum_{d=1}^{D} (|z_d|^2+\beta)^{\frac{1}{2}}, \quad (34)$$

where d indexes the elements of vector z, $D = IQ$, and β is a nonnegative small constant. Here, we choose $\beta = 0.01$. In the first step of the $p+1$th iteration, the estimation of imaging result vector z is obtained as

$$\hat{z}^{(p+1)} = W^{-1}(\hat{z}^{(p)}) M_2^H e^{j\hat{\Phi}^p} M_1^H y, \quad (35)$$

where explicit expression of $W(z)$ in (36), shown at the top of this page.

In the second step of the $p+1$th iteration, the estimation of phase error matrix $\hat{\Phi}^{(p+1)}$ is

$$\hat{\Phi}^{(p+1)} = arg\min_{\Phi} J, \quad (37)$$

where J is the cost function to be minimized in the second step

$$J = \left\| y - M_1 e^{-j\hat{\Phi}^p} M_2 \hat{z}^{p+1} \right\|_2^2. \quad (38)$$

To solve the optimization problem in (37), a Newton's method is utilized. The explicit expression of the gradient should be obtained first

$$\nabla J(\Phi) = \begin{bmatrix} \frac{\partial J}{\partial \Phi_1} & & & \\ & \frac{\partial J}{\partial \Phi_2} & & \\ & & \ddots & \\ & & & \frac{\partial J}{\partial \Phi_D} \end{bmatrix}. \quad (39)$$

To calculate the gradient in (39), the key point is to derive $\frac{\partial J}{\partial(\Phi_b)}$ for any $b = 1, 2, \cdots, D$,

$$\begin{aligned} \frac{\partial J}{\partial \Phi_b} &= \frac{\partial}{\partial \Phi_b}(-2\mathrm{Re}\{y^H M_1 e^{-j\Phi} M_2 \hat{z}^{p+1}\}) \\ &= -Im\{\sum_{d=1}^{D} j y_b' e^{-j\Phi_b} (M_2)_{b,d} (\hat{z}^{p+1})_d\}, \end{aligned} \quad (40)$$

where vector y' is

$$y' = \left[\sum_{d=1}^{D} y_d^* (M_1)_{d,1} \ \sum_{d=1}^{D} y_d^* (M_1)_{d,2} \ \cdots \ \sum_{d=1}^{D} y_d^* (M_1)_{d,D} \right]. \quad (41)$$

Then, to utilize the Newton's method, the Hessian matrix $H_e(\Phi)$ should be derived. According to (40), we can get that, if $b \neq d$,

$$\frac{\partial^2 J}{\partial \Phi_b \partial \Phi_d} = 0. \quad (42)$$

Therefore, $H_e(\Phi)$ is a diagonal matrix, which can be written as

$$H_e(\Phi) = \begin{bmatrix} \frac{\partial^2 J}{\partial \Phi_1^2} & & & \\ & \frac{\partial^2 J}{\partial \Phi_2^2} & & \\ & & \ddots & \\ & & & \frac{\partial^2 J}{\partial \Phi_D^2} \end{bmatrix}. \quad (43)$$

In (43), for any $b = 1, 2, \cdots, D$, $\frac{\partial^2 J}{\partial \Phi_b^2}$ can be calculated as

$$\frac{\partial^2 J}{\partial \Phi_b^2} = Re\{\sum_{d=1}^{D} j y_b' e^{-j\Phi_b} (M_2)_{b,d} (\hat{z}^{p+1})_d\}. \quad (44)$$

According to the theory of Newton's method [39], [40], the updating rule of phase error matrix Φ in the $p+1$th iteration is

$$\hat{\Phi}^{p+1} = \hat{\Phi}^p - [H_e(\hat{\Phi}^p)]^{-1} \nabla J(\hat{\Phi}^p). \quad (45)$$

C. COMPUTATIONAL COMPLEXITY

According to the block coordinate descent optimization scheme, the proposed method is an iterative approach with two steps in each iteration. In the estimation of imaging result vector shown in (35), we need to 3 times of block diagnose matrix multiplication and a multiplication between block diagnose matrix with vector. Supposing that $N_a = N_r = N$, the number of real floating point operations of (35) is $4N^3$. Inspecting (45), we need calculate a diagonal matrix inversion, a diagonal matrix multiplication and a diagonal matrix addition in the estimation of the correction phases. Therefore the number of real floating point operations of (45) is $3N^2$. The total number of real floating point operations of the proposed method is $4N^3 + 3N^2$, and the computation complexity of the proposed method is of order $O(N^3)$.

Compared with the conventional frequency domain imaging method such as RD, CS and Omega-K of complexity order $O(N^2 log_2 N)$, the proposed method is a little less computational efficient. But comparatively, the proposed method has the advantage of less sampling amount, super resolution, sidelobe suppression,. etc. It's a trade-off.

In the sparsity-driven autofocus method based on the exact observation model in [27], all the elements of the system matrix are non-zero. Therefore, the computational complexity of the autofocus method based on exact observation model is of order $O(N^6)$, which is much larger than the proposed method.

D. DISCUSSION

It is worth noting that the proposed imaging and motion compensation scheme takes the simplest imaging algorithm RD as an example. Some other imaging algorithms such as CS, Omega-k also can be utilized in the proposed imaging and motion compensation scheme. The matrixes M_1 and M_2 are different, but the other processes stay the same. Therefore, we can choose the imaging algorithm according to actual requirement. In addition, the proposed imaging and motion compensation scheme can be applied in different SAR systems, such as squinted SAR, Bistatic SAR,. etc, by changing the imaging algorithm.

V. RESULTS

In this section, processing of simulation and experimental SAR data is presented to verify the effectiveness of the proposed method. For comparison, the RD imaging algorithm with map drift (MD) [21], minimum entropy autofocus [23] and range-dependent phase gradient algorithm (PGA) [13], the fast CS-based imaging using the inversion of RD algorithm without motion compensation, the CS-based method using exact observation model with 2-dimensional autofocus in [27], the sparsity-driven autofocusing in [29] and the proposed method are utilized.

A. SIMULATION

In this subsection, the effectiveness of the proposed method is verified by simulation results. In the simulation, to simulate the experimental SAR data, motion errors are added during SAR echo generation. The relevant geometry and system parameters are shown in Table 1. To verify the effectiveness of the proposed CS-driven autofocus method, we perform a random selection on the uniform sampled data with 60% sampling rate.

TABLE 1. Simulation parameters.

Geometry Parameters	Squint angle of the platform	22.6^0
	Initial location of the platform	(–4, –3, 6)km
	Velocity	80m/s
System Parameters	Carrier frequency	10GHz
	Wavelength	0.03m
	Bandwidth	150MHz
	Pulse repetition frequency	2000Hz

Fig. 8 shows the imaging results. The imaging results by the RD imaging algorithm with MD, minimum entropy autofocus and range-dependent PGA, the fast CS-based imaging using the inversion of RD algorithm without motion compensation, the sparsity-driven autofocusing in [29], the CS-based method using exact observation model with 2-dimensional autofocus and the proposed method are illustrated in Fig. 8(a)-(g), respectively.

For the imaging result by the conventional RD algorithm with different autofocus as shown in Fig. 8(a), (b), and (c) the imaging results are unfocused due to the SAR echo is randomly sampled. In Fig. 8(d), it can be observed that the imaging result suffers from severe defocus due to the influence of motion errors. In Fig. 8(e), the motion errors are partially removed, and the image quality is slightly improved. However, due to the high-order terms and the spatial-variance of the motion errors, the imaging result in Fig. 8(e) is obviously not well-focused. Comparatively, the imaging result in Fig. 8(f) is well-focused by the CS-based method using exact observation model with 2-dimensional autofocus. From Fig. 8 (f), it can be observed that by using the CS-based method using exact observation model with 2-dimensional autofocus, we can eliminate the influence of motion errors and get the well focused SAR image. The imaging result by the proposed approach is shown in Fig. 8 (g). We can find that, by using the proposed approach as well as the CS-based method using exact observation model with 2-dimensional autofocus, all the targets in the scene can be well focused. The range-variant motion errors are accurately corrected.

Then, the imaging qualities of these three methods are analyzed quantitatively as shown in Table 2. The target-background ratio (TBR), impulse-response width (IRW), peak sidelobe ratio (PSLR), and integrated sidelobe ratio (ISLR) of target A in azimuth direction are utilized to measure the imaging quality, where target A is a randomly selected target in Fig. 8 (a)-(g), and its position is shown in Fig. 8 (f). We define TBR as

$$TBR = 20\log_{10}\left(\frac{\max\limits_{z_i \in Target} |z_i|}{(1/N_{bg}) \sum\limits_{z_i \in Backgroud} |z_i|}\right), \tag{46}$$

where N_{bg} represents the number of pixels in the background. As a consequence, we can distinguish the target from the background more easily with the higher TBR. The imaging qualities are shown in Table 2.

From Table 2, it can be observed that the TBRs of the proposed method and CS-based method using exact observation model with 2-dimensional autofocus are larger than the other methods. Similar with TBR, other imaging qualities of these two methods are performed better than the other methods. In comparison, the proposed method has almost the same imaging quality as the CS based method using exact observation model with 2-dimensional autofocus. As analyzed in [28] and [30], in the CS-based imaging algorithms, we can have the advantage of side-lobe suppression in the final imaging results. Accordingly, the IRW, PSLR and ISLR of the proposed method are much smaller than the theoretical values, -13.27dB and -10.23dB, respectively.

Then, we compare the CPU time of different methods. To measure the processing times, the methods have been implemented in Matlab version R2012 b and on a computer with a 3.10-GHz Intel processor and 4-GB RAM. The running time of he RD imaging algorithm with MD, minimum entropy autofocus and range-dependent PGA, the fast CS-based imaging using the inversion of RD algorithm

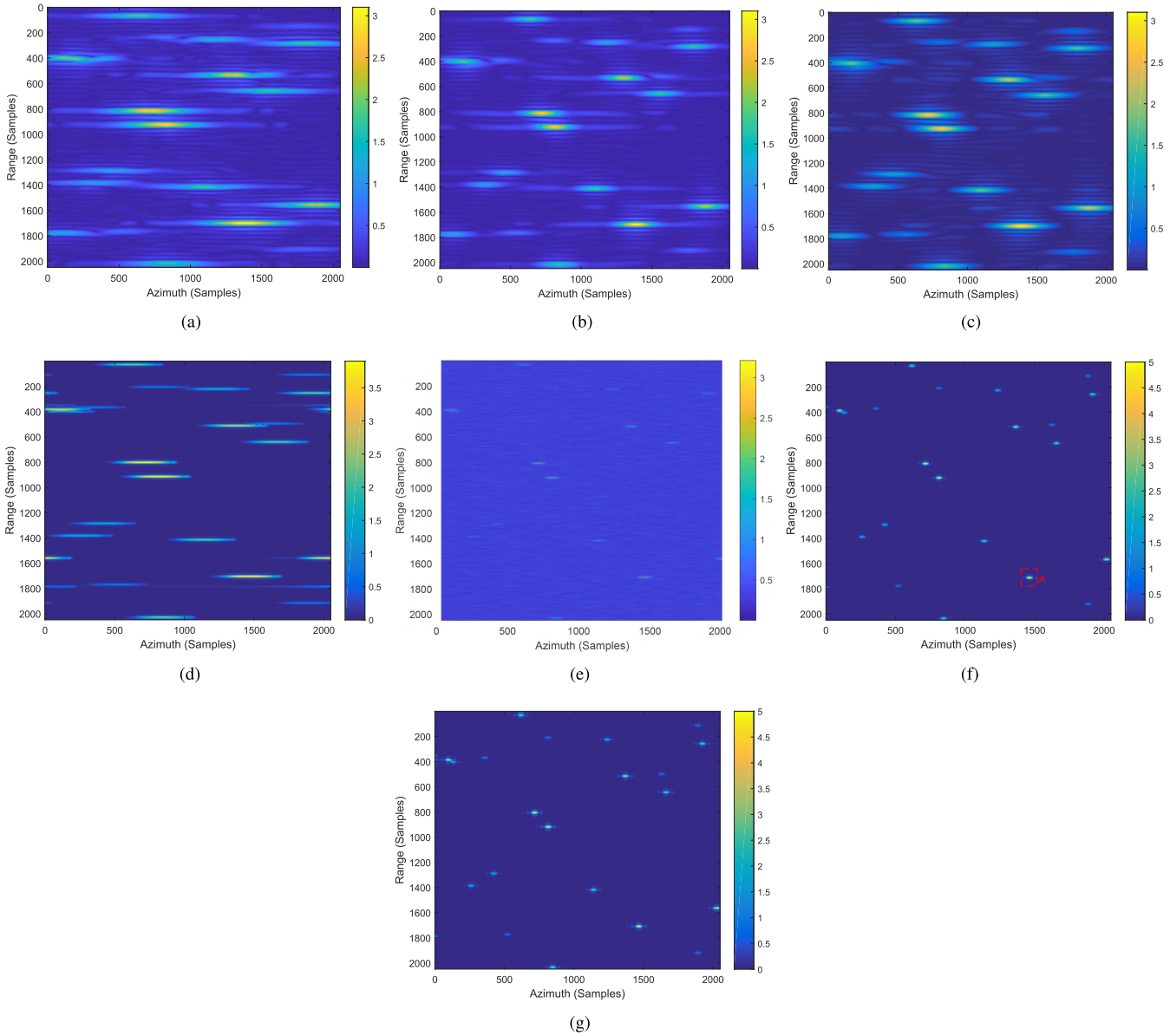

FIGURE 8. Imaging results of the simulation. (a) By the RD imaging algorithm with MD. (b) By the RD imaging algorithm with minimum entropy autofocus. (c) By the RD imaging algorithm with range-dependent PGA. (d) By the fast CS-based imaging using the inversion of RD algorithm without motion compensation. (e) By the sparsity-driven autofocusing in [29]. (f) By the CS-based method using exact observation model with 2-dimensional autofocus. (g) By the proposed method.

TABLE 2. Imaging quality of the simulation.

	(a)	(b)	(c)	(d)	(e)	(f)	(g)
TBR(dB)	40.2	44.5	49.8	27.4	60.3	83.4	86.7
IRW(m)	2.57	1.95	1.83	3.11	0.51	0.32	0.26
PSLR(dB)	-8.6	-9.2	-9.8	-7.2	-20.2	-27.3	-36.9
ISLR(dB)	-7.3	-8.1	-8.5	-5.9	-17.8	-26.8	-32.5

without motion compensation, the sparsity-driven autofocusing in [29], the CS-based method using exact observation model with 2-dimensional autofocus and the proposed method are 19.34s, 20.45s, 28.49s, 50.89s, 79.64s, 247.82s, and 64.24s, respectively. The proposed method is much faster than the CS based method using exact observation model

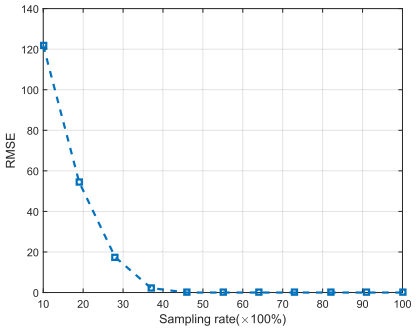

FIGURE 9. RMSE with different sampling rate.

TABLE 3. Parameters for the experiment.

Geometry Parameters	Squint angle of the platform	62.0^0
	Initial location of the platform	$(-3,-8,3)$km
	Velocity	120m/s
System Parameters	Carrier frequency	10GHz
	Wavelength	0.03m
	Bandwidth	300MHz
	Pulse repetition frequency	1200Hz

with 2-dimensional autofocus while keeping the imaging accuracy.

The RMSE of the proposed method varying with sampling rates is presented in Fig. 9. It can be seen that the proposed method can obtain highly accurate imaging result when the sampling rate is larger than 25%, which verifies that the proposed method has the advantage of not requiring to much sampling amount compared with the conventional imaging algorithm.

B. EXPERIMENT

A set of real data, whose geometry resolution is 0.75×0.8m (range $\times$ azimuth), is collected by an X-band SAR system works in strip-map mode in this subsection. In this experiment, the relevant geometry and system parameters are shown in Table 3. Similar with the random sampling in the subsection of simulation, to verify the effectiveness of the proposed CS-driven autofocus method, we perform a random selection on the uniform sampled data with 70% sampling rate.

Fig. 10 shows the imaging results of the experimental data. The horizontal direction is azimuth, and the vertical direction is range. The imaging results by the RD imaging algorithm with MD, minimum entropy autofocus and range-dependent PGA, the fast CS-based imaging using the inversion of RD algorithm without motion compensation, the sparsity-driven autofocusing in [29] and the proposed method are illustrated in Fig. 10(a)-(f), respectively.

Similar to the imaging results in Fig. 8, the experimental results by the conventional RD algorithm with different autofocus methods are defocused for the sake of randomly sampled echo. As shown in Fig.10(d), it can be seen that the imaging result by the fast CS-based imaging algorithm without motion compensation is defocused. As there is no motion

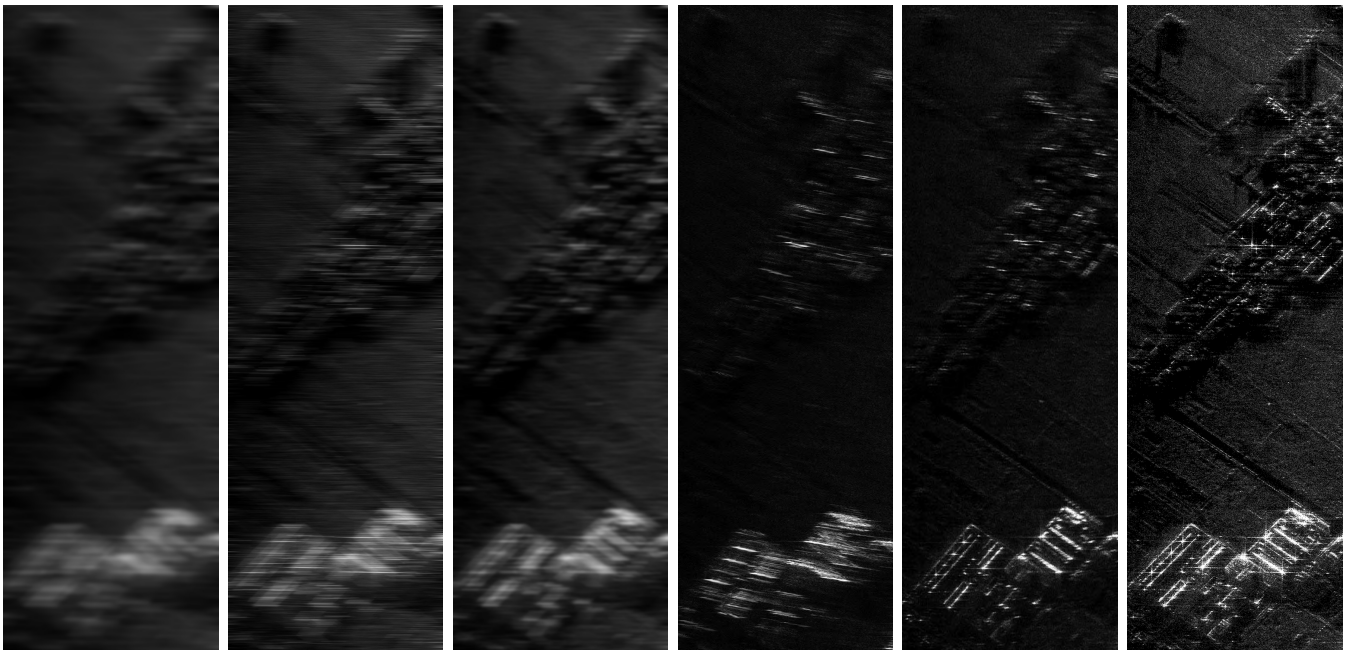

FIGURE 10. Imaging results of the experiment. (a) By the RD imaging algorithm with MD. (b) By the RD imaging algorithm with minimum entropy autofocus. (c) By the RD imaging algorithm with range-dependent PGA. (d) By the fast CS-based imaging using the inversion of RD algorithm without motion compensation. (e) By the sparsity-driven autofocusing in [29]. (f) By the proposed method.

compensation processing, the appearance of the buildings, roads and forest are seriously blurred. As shown in Fig. 10(e), the focusing quality evidently improves by the sparsity-driven autofocusing in [29]. However, in Fig. 10(e), the building on the bottom of the image is focused, while the forest area on the top of the image is unfocused due to the range-variance and the high-order terms of the motion errors. In Fig.10(f), the imaging quality using the proposed algorithm is evidently improved. The details of the buildings, forest and roads in the whole image are clear. Moreover, the entropies of the images in Fig. 10 is calculated to evaluate the imaging quality. The smaller entropy is, the better focused quality we have. The entropies of Fig. 10(a)-(f) are 13.05, 11.72, 11.38, 11.19, 10.94 and 10.43, respectively. We have the smallest entropy by using the proposed method. It can be concluded from the experimental results that compared with the other methods, the proposed method has a better performance.

VI. CONCLUSION

In this paper, a fast CS-based imaging algorithm integrated with motion error compensation is proposed. Firstly, the spatial-variance property of motion errors in SAR system is analyzed, and we can get the conclusion that range-variance of the motion errors should be taken into consideration and the azimuth-variance could be neglected. Then, a CS-based imaging model using the inversion observation of RD algorithm combined with range-variant compensation is established. Accordingly, the imaging and motion compensation problem is transformed into an optimization problem. A block coordinate descent scheme is utilized to solve the optimization problem, and the range-variant phase errors and imaging results are estimated iteratively. In contrast to the existing fast CS-based imaging methods, as the spatially-variant motion errors have been compensated, the imaging quality of the proposed method has been greatly improved. Simulation and experimental results verify the effectiveness of the proposed method.

REFERENCES

[1] J. Wu, W. Pu, Y. Huang, J. Yang, and H. Yang, "Bistatic forward-looking SAR focusing using $\omega-\kappa$ based on spectrum modeling and optimization," *IEEE J. Sel. Topics Appl. Earth Observ. Remote Sens.*, vol. 11, no. 11, pp. 4500–4512, Nov. 2018.

[2] J. Wu *et al.*, "Two-dimensional frequency decoupling method for curved trajectory synthetic aperture radar imaging," *IET Radar, Sonar Navigat.*, vol. 12, no. 7, pp. 766–773, Jun. 2018.

[3] J. Wu, Z. Sun, H. An, J. Qu, and J. Yang, "Azimuth signal multichannel reconstruction and channel configuration design for geosynchronous spaceborne—Airborne bistatic SAR," *IEEE Trans. Geosci. Remote Sens.*, vol. 57, no. 4, pp. 1861–1872, Apr. 2019.

[4] E. J. Candès, J. Romberg, and T. Tao, "Robust uncertainty principles: Exact signal reconstruction from highly incomplete frequency information," *IEEE Trans. Inf. Theory*, vol. 52, no. 2, pp. 489–509, Feb. 2006.

[5] E. J. Candès and T. Tao, "Near-optimal signal recovery from random projections: Universal encoding strategies?" *IEEE Trans. Inf. Theory*, vol. 52, no. 12, pp. 5406–5425, Dec. 2006.

[6] D. L. Donoho, "Compressed sensing," *IEEE Trans. Inf. Theory*, vol. 52, no. 4, pp. 1289–1306, Apr. 2006.

[7] J. H. G. Ender, "On compressive sensing applied to radar," *Signal Process.*, vol. 90, no. 5, pp. 1402–1414, May 2010.

[8] L. C. Potter, E. Ertin, J. T. Parker, and M. Cetin, "Sparsity and compressed sensing in radar imaging," *Proc. IEEE*, vol. 98, no. 6, pp. 1006–1020, Jun. 2010.

[9] H. Bu, R. Tao, X. Bai, and J. Zhao, "A novel SAR imaging algorithm based on compressed sensing," *IEEE Geosci. Remote Sens. Lett.*, vol. 12, no. 5, pp. 1003–1007, May 2015.

[10] S. Samadi, M. Cetin, and M. A. Masnadi-Shirazi, "Sparse representation-based synthetic aperture radar imaging," *IET Radar, Sonar Navigat.*, vol. 5, no. 2, pp. 182–193, Feb. 2011.

[11] M. Çetin *et al.*, "Sparsity-driven synthetic aperture radar imaging: Reconstruction, autofocusing, moving targets, and compressed sensing," *IEEE Signal Process. Mag.*, vol. 31, no. 4, pp. 27–40, Jul. 2014.

[12] W. Pu, W. Li, J. Wu, Y. Huang, J. Yang, and H. Yang, "An azimuth-variant autofocus scheme of bistatic forward-looking synthetic aperture radar," *IEEE Geosci. Remote Sens. Lett.*, vol. 14, no. 5, pp. 689–693, May 2017.

[13] M. Xing, X. Jiang, R. Wu, F. Zhou, and Z. Bao, "Motion compensation for UAV SAR based on raw radar data," *IEEE Trans. Geosci. Remote Sens.*, vol. 47, no. 8, pp. 2870–2883, Aug. 2009.

[14] A. Moreira and Y. Huang, "Airborne SAR processing of highly squinted data using a chirp scaling approach with integrated motion compensation," *IEEE Trans. Geosci. Remote Sens.*, vol. 32, no. 5, pp. 1029–1040, Sep. 1994.

[15] W. Pu *et al.*, "Motion errors and compensation for bistatic forward-looking SAR with cubic-order processing," *IEEE Trans. Geosci. Remote Sens.*, vol. 54, no. 12, pp. 6940–6957, Dec. 2016.

[16] L. Zhang, Z. Qiao, M.-D. Xing, L. Yang, and Z. Bao, "A robust motion compensation approach for UAV SAR imagery," *IEEE Trans. Geosci. Remote Sens.*, vol. 50, no. 8, pp. 3202–3218, Feb. 2012.

[17] W. Pu *et al.*, "A rise-dimensional modeling and estimation method for flight trajectory error in bistatic forward-looking SAR," *IEEE J. Sel. Topics Appl. Earth Observ. Remote Sens.*, vol. 10, no. 11, pp. 5001–5015, Sep. 2017.

[18] W. Pu *et al.*, "Nonsystematic range cell migration analysis and autofocus correction for bistatic forward-looking SAR," *IEEE Trans. Geosci. Remote Sens.*, vol. 56, no. 11, pp. 6556–6570, Nov. 2018.

[19] D. E. Wahl, P. Eichel, D. C. Ghiglia, and C. V. Jakowatz, "Phase gradient autofocus-a robust tool for high resolution SAR phase correction," *IEEE Trans. Aerosp. Electron. Syst.*, vol. 30, no. 3, pp. 827–835, Jul. 1994.

[20] W. Pu, J. Wu, X. Wang, Y. Huang, Y. Zha, and J. Yang, "Joint sparsity-based imaging and motion error estimation for BFSAR," *IEEE Trans. Geosci. Remote Sens.*, vol. 57, no. 3, pp. 1393–1408, Mar. 2019. doi: 10.1109/TGRS.2018.2866437.

[21] P. Samczynski and K. S. Kulpa, "Coherent mapdrift technique," *IEEE Trans. Geosci. Remote Sens.*, vol. 48, no. 3, pp. 1505–1517, Mar. 2010.

[22] Y. Gao, W. Yu, Y. Liu, R. Wang, and C. Shi, "Sharpness-based autofocusing for stripmap SAR using an adaptive-order polynomial model," *IEEE Geosci. Remote Sens. Lett.*, vol. 11, no. 6, pp. 1086–1090, Jun. 2014.

[23] T. Xiong, M. Xing, Y. Wang, S. Wang, J. Sheng, and L. Guo, "Minimum-entropy-based autofocus algorithm for SAR data using chebyshev approximation and method of series reversion, and its implementation in a data processor," *IEEE Trans. Geosci. Remote Sens.*, vol. 52, no. 3, pp. 1719–1728, Mar. 2014.

[24] K. H. Liu and D. C. Munson, "Fourier-domain multichannel autofocus for synthetic aperture radar," *IEEE Trans. Image Process.*, vol. 20, no. 12, pp. 3544–3552, Dec. 2011.

[25] K.-H. Liu, A. Wiesel, and D. C. Munson, "Synthetic aperture radar autofocus based on a bilinear model," *IEEE Trans. Image Process.*, vol. 21, no. 5, pp. 2735–2746, May 2012.

[26] K.-H. Liu, A. Wiesel, and D. C. Munson, "Synthetic aperture radar autofocus via semidefinite relaxation," *IEEE Trans. Image Process.*, vol. 22, no. 6, pp. 2317–2326, Jun. 2013.

[27] S. Kelly, M. Yaghoobi, and M. Davies, "Sparsity-based autofocus for undersampled synthetic aperture radar," *IEEE Trans. Aerosp. Electron. Syst.*, vol. 50, no. 2, pp. 972–986, Apr. 2014.

[28] N. Ö. Onhon and M. Cetin, "A sparsity-driven approach for joint SAR imaging and phase error correction," *IEEE Trans. Image Process.*, vol. 21, no. 4, pp. 2075–2088, Apr. 2012.

[29] Y.-C. Chen, G. Li, Q. Zhang, Q.-J. Zhang, and X.-G. Xia, "Motion compensation for airborne SAR via parametric sparse representation," *IEEE Trans. Geosci. Remote Sens.*, vol. 55, no. 1, pp. 551–562, Jan. 2017.

[30] X. Dong and Y. Zhang, "A novel compressive sensing algorithm for SAR imaging," *IEEE J. Sel. Topics Appl. Earth Observ. Remote Sens.*, vol. 7, no. 2, pp. 708–720, Feb. 2014.

[31] J. Fang, Z. Xu, B. Zhang, W. Hong, and Y. Wu, "Fast compressed sensing SAR imaging based on approximated observation," *IEEE J. Sel. Topics Appl. Earth Observ. Remote Sens.*, vol. 7, no. 1, pp. 352–363, Jan. 2014.
[32] S. Chen, D. Donoho, and M. Saunders, "Atomic decomposition by basis pursuit," *SIAM Rev.*, vol. 43, no. 1, pp. 129–159, 2001.
[33] D. L. Donoho and X. Huo, "Uncertainty principles and ideal atomic decomposition," *IEEE Trans. Inf. Theory*, vol. 47, no. 7, pp. 2845–2862, Nov. 2001.
[34] E. Candes, J. Romberg, and T. Tao, "Satble signal recovery from incomplete and inaccurate measurements," *J. Inst. Math. Sci.*, vol. 59, no. 8, pp. 1207–1223, Aug. 2006.
[35] R. G. Baraniuk, "Compressive sensing," *IEEE Signal Process. Mag.*, vol. 24, no. 4, pp. 118–121, Jul. 2007.
[36] Z. M. Wang and W. W. Wang, "Fast and adaptive method for sar super-resolution imaging based on point scattering model and optimal basis selection," *IEEE Trans. Image Process.*, vol. 18, no. 7, pp. 1477–1486, Jul. 2009.
[37] G. Fornaro, G. Franceschetti, and S. Perna, "On center-beam approximation in SAR motion compensation," *IEEE Geosci. Remote Sens. Lett.*, vol. 3, no. 2, pp. 276–280, Apr. 2006.
[38] Z. Xu, X. Chang, F. Xu, and H. Zhang, "$L_{1/2}$ regularization: A thresholding representation theory and a fast solver," *IEEE Trans. Neural Netw. Learn. Syst.*, vol. 23, no. 7, pp. 1013–1027, Jul. 2012.
[39] Y. Sun, S. Zhang, and Z. Cui, "Group sparsity based imaging algorithm for TWRI under wall parameter uncertainties," *Trans. Inst. Meas. Control*, vol. 40, no. 1, pp. 251–260, 2018. doi: 10.1177/0142331216652467.
[40] H. Raja, W. U. Bajwa, and F. Ahmad, "Through-the-wall radar imaging using a distributed quasi-Newton method," in *Proc. 51st Asilomar Conf. Signals, Syst., Comput.*, Nov. 2017, pp. 85–89.

WEI PU (S'12) received the B.S. degree in electronic engineering from the University of Electronic Science and Technology of China, in 2012, where he is currently pursuing the Ph.D. degree in bistatic SAR imaging and motion compensation. His research interests include synthetic aperture radar and sparse signal processing.

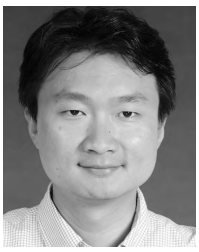

YULIN HUANG (S'06–M'08) received the B.S. and Ph.D. degrees in electronic engineering from the University of Electronic Science and Technology of China, Chengdu, China, in 2002 and 2008, respectively, where he is currently a Professor. His research interests include signal processing and radar imaging.

JUNJIE WU (S'06–M'13) received the B.S., M.S., and Ph.D. degrees in electronic engineering from the University of Electronic Science and Technology of China, Chengdu, China, in 2004, 2007, and 2013, respectively, where he is currently an Associate Professor.

HAIGUANG YANG (S'06–M'09) received the B.S. and Ph.D. degrees in electronic engineering from the University of Electronic Science and Technology of China, Chengdu, China, in 2001, and 2013, respectively, where he is currently an Associate Professor. His research interests include signal processing and synthetic aperture radar.

JIANYU YANG (M'06) received the B.S. degree in electronic engineering from the National University of Defense Technology, Changsha, China, in 1984, and the M.S. and Ph.D. degrees in electronic engineering from the University of Electronic Science and Technology of China (UESTC), Chengdu, in 1987 and 1991, respectively.

He is currently a Professor with the School of Electronic Engineering, UESTC. His research interests include synthetic aperture radar and statistical signal processing.